

Self-learning signal classifier for decameter coherent scatter radars

Oleg Berngardt Ivan Lavygin et al.

Abstract

The paper presents a method for automatic constructing a classifier for processed data obtained by decameter coherent scatter radars. Method is based only on the radar data obtained, the results of automatic modeling of radio wave propagation in the ionosphere, and mathematical criteria for estimating the quality of the models. The final classifier is the model trained at data obtained by 12 radars of the SuperDARN and SECIRA networks over two years for each radar. The number of the model coefficients is 2669. For the classification, the model uses both the calculated parameters of radio wave propagation in the model ionosphere and the parameters directly measured by the radar. Calibration of radiowave elevation measurements at each radar was made using meteor trail scattered signals. The analysis showed that the optimal number of classes in the data is 37, of which 25 are frequently observed. The analysis made it possible to choose 14 classes from them, which are confidently separated in other variants of model training. A preliminary interpretation of 10 of them was carried out. The dynamics of observation of various classes and their dependence on the geographical latitude of radars at different levels of solar and geomagnetic activity were presented, it was shown that it does not contradict with known physical mechanisms. The analysis showed that the most important parameters to identify the classes are the shape of the signal ray-tracing trajectory in its second half, the ray-traced scattering height and the Doppler velocity measured by the radar.

1 Introduction

Decameter coherent scatter radars are currently popular and highly informative instruments for monitoring the state of the ionosphere at high and mid-latitudes. The largest network of these radars today is SuperDARN - Super Dual Auroral Radar Network, [15, 13, 23]. There are also CN-DARN[34] and SECIRA[4] networks growing. The features of the radars are their short-wave radio frequency range, allowing long-range (multihop) propagation of radio waves, significantly expanding the radar range upto 3-4 thousand kilometers and increasing the number of effects affecting the radiowave propagation, but complicating the interpretation of the received signals[23].

The first stage of interpreting the signals is their classification - separating them into classes based on their characteristics. The one of the oldest and simplest methods of the classification is separating them into ionospheric scattering

and scattering from the earth's surface (groundscatter), traditionally carried out by the spectral width of the received signal and its Doppler velocity [26]. Due to the large number of different signal types[23], the classification is not complete and requires improvement. Recent approaches include the use of statistical methods for separating the two classes [10, 21], the use of clustering for taking into account the spatio-temporal distribution of the signals [28], the use of neural networks and clustering methods to identify complex dependencies and classes [20, 19]. Most of these approaches are based on separating the signals into initially predefined classes.

Another approach to solving this problem is proposed in [8] and developed in [2, 3] - a method for separating signals into initially unknown classes. It is performed within the framework of self-learning neural networks - the superposition of unsupervised and supervised machine learning methods, with subsequent interpretation of the resulting classes by researcher after final network train. This approach refers to data-driven analysis methods and is based on the use of the experimental data only to build an optimal classification model automatically, by reducing researcher influence.

Previously, these works were carried out only for the SECIRA network radars[8, 2, 3]. The proposed paper is a generalization of this approach. We attempt to further reduce the influence of the researcher on the process of constructing the model and to generalize the model to the periods of different solar activity and different radar locations.

We also study the dependence of observed signal classes on geophysical conditions and radar location, as well as importance of different measured signal parameters on classification accuracy.

The proposed classifier model (Encoder in Fig.1A) is a neural network of an extremely simple architecture (two fully connected layers), sufficient to solve the problem. Its architecture is shown in Fig.1C. The main difficulty of this approach is the process of classifier training, which includes building a huge model (multi-head autoencoder) based on it, each head of which is trained independently in independent experiments. The network teacher (labeler) in this case is a clusterer - a method for separating signals into groups (clusters) without a teacher. This approach was proposed in [8] and was referred as 'wrapped classifier' to highlight the fact that to train a classifier, it is necessary to train a more complex neural network ('wrap'), of which this classifier will be only a small part.

The architecture of autoencoder networks is quite popular and allows extracting internal (latent) representations from data - the implicit (hidden) independent parameters that describe the studied data well [31]. As shows our analysis this architecture has demonstrated its effectiveness for solving our classification problem. A detailed architecture of the used autoencoder is shown in Fig.1B. The autoencoder is a significantly optimized and reduced version of the models [8, 2], proposed and described in detail in [3].

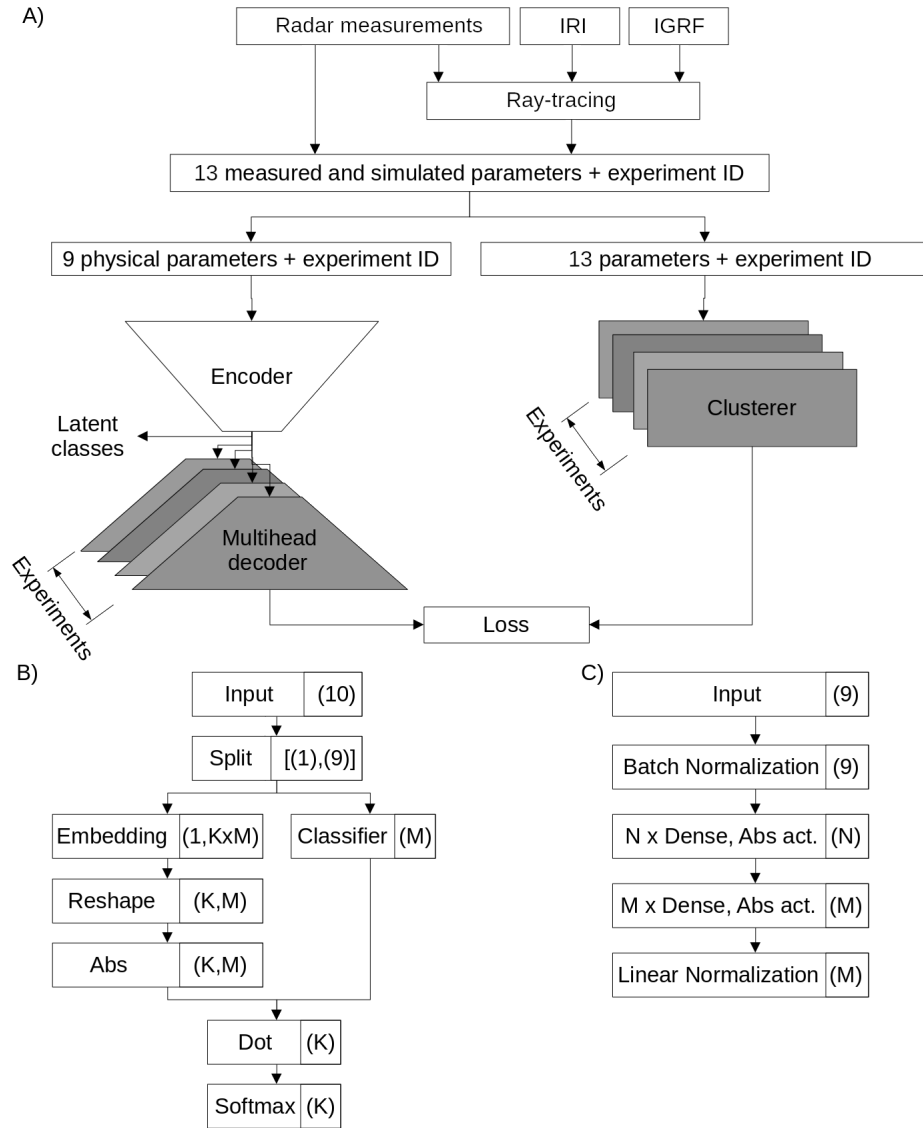


Fig. 1: A) Neural network architecture and its training method. Different colors corresponds to different experiments. Number of decoder heads and clusterers is about 4000; B) Implementation of a multi-head autoencoder; C) Implementation of the Encoder (classifier).

2 Preliminary data preparation

2.1 Initial data and training

Coherent scatter radars are over-the-horizon radars[15], that transmit pulse sounding sequences at frequencies in range 8-20MHz, and estimate the parameters of backscattered signals, as a function of time, delay(radar range) and transmit/receive azimuth. The parameters are estimated by accumulating autocorrelation function (ACF) of the signals received by two spatially separated antenna arrays to measure elevation angle of radiowave too. The measured ACFs are averaged over 2-6 seconds and processed by FITACF algorithm[29]. Each signal (measurement), measured at given time, range and azimuth has its own power and spectral characteristics, as well as elevation angle of the trajectory of received radiowave. These parameters and their spatio-temporal distribution are used later by researchers for the signal interpretation.

The following measured and model parameters were used to construct the neural network classifier of the signals.

The parameters directly measured by the radar are:

- 1) Universal time and radar range;
- 2) Measured doppler velocity V and spectral width W, calculated from the received signals using the FITACF algorithm [29], in the paper we use spectral width in the exponential model of the correlation function (W1);
- 3) Measured elevation angle of the received radiowave - determined by the algorithm [7] after calibrating the radar using meteor trail scattered signals;
- 4) Effective scattering height - calculated based on the elevation angle and range as a result of refraction-free radio wave propagation.

The parameters obtained as a result of radio wave propagation simulation using direct radar measurements and the geometric optics method (ray-tracing) in the IRI-2020[9] model ionosphere are:

- 5) Trajectory elevation relative to the horizon at 4 points over the range (1/4,2/4,3/4,4/4 of the measured range, we use sine of the elevation angle);
- 6) Angle between the direction of radio wave trajectory and the Earth's magnetic field at the scattering point - calculated from the reference magnetic field model IGRF[33], we use cosine of the angle;
- 7) Propagation mode - the number of reflections (hops) from the underlying layer (the earth's surface or the ionospheric layer in the case of interlayer waveguide propagation) during propagation to the scatterer;
- 8) Scattering height.

Only 9 of these parameters were used as input data for the classifier: velocity and spectral width, trajectory shape, angle with the magnetic field, propagation mode, and scattering height. Whole 13 parameters were used for clustering only. To train the model we separated all available data into experiments. Each experiment corresponds to the data for a selected radar, day, channel, azimuth (beam) of transmission, and sounding frequency (with an accuracy of 1 MHz). To reduce the amount of data and speed up calculations, only 3% of all available

experiments were randomly selected. To limit the amount of the data, no more than 5000 measurements (signals with a power of 3 dB above the noise level) were randomly selected from each experiment. This gave us about 24 mln. unique unlabeled measurements in 5566 unique experiments for training the classification model.

The clusterer used is a modeling of the single experiment data distribution by a mixture of multidimensional Gaussian distributions (Gaussian Mixture)[1] with the number of clusters determined from the minimum of the Bayesian information criterion (BIC)[32], each experiment has its own number of found clusters.

As a classifier we use two-layer neural network with absolute activation functions, chosen, among other things, to provide the continuity with existing generally used approach of separating the signals into two classes [26] and to follow the Kolmogorov-Arnold representation theorem [18] allowing approximating a wide class of solutions by using two-layer networks only. Linear normalization of the sum was used as output balancing for interpreting the results as class probabilities. The choice of classifier and clusterer architecture is discussed in more detail in [3].

2.2 Radars and their elevation calibration

The methods that take into account radio wave propagation requires accurate elevation angle measurements, and their precise calibration. The elevation calibration in our case was made using signals scattered by meteor trails. The method was proposed for SuperDARN radars in [12]. We use a modification of the algorithm described in [7], and based on calibrating the radar at each sounding frequency separately, determining the scattering height for each meteor, and analyzing the expected and measured phase between signals received by two spatially separated phased arrays of the radar, calculated by FITACF algorithm. In this paper, a small change was made to the algorithm: all meteor trails were assumed to be observed at 104 km height. This is related with large amount of calculations (data of all available radars over two years, with sounding frequency discrete 200 kHz for calibration). So only averaged (processed) data, with significantly smaller amount than non-averaged IQ components of signals, can be used for calibration. This does not allow direct use of the [7] method for determining the scattering altitude by the meteor trail lifetime, that could be calculated by IQ components of the signal only. The disadvantage of this modification is systematic errors associated with neglected deviation of the scattering height from actual one, and the advantage is the calculation speed. In this case, we also assume that the scattering altitudes do not depend on the geographical location and time, which can also affects to the calibration accuracy. Nevertheless, these assumptions allow us to unify the calibration of all the radars.

During calibration, we select the signals detected by the FITACF algorithm[29], with low Doppler velocities (less than 50 m/s), high signal-to-noise ratios (above 3dB), and from near radar ranges (not exceeding 350 km) were considered as

Tab. 1: Radars, their latitudes, and data years used in the research

Radar	Lat.	Years	Radar	Lat.	Years
CVE SuperDARN	43.3N	2020,2023	CVW SuperDARN	43.3N	2020,2023
EKB SECIRA	56.5N	2021,2023	HOK SuperDARN	43.5N	2020,2023
KAP SuperDARN	49.4N	2020,2023	MAGW SECIRA	60.0N	2021,2024
MCM SuperDARN	77.8S	2014,2020	PGR SuperDARN	54.0N	2020,2023
PYK SuperDARN	63.8N	2010,2014	SAS SuperDARN	52.2N	2020,2023
SPS SuperDARN	90.0S	2014,2021	STO SuperDARN	63.9N	2011,2014

scattering by meteor trails. All the radars available for the analysis were calibrated, of which 12 radars were selected. The radars are summarized in Table 1, their locations are shown in Fig.2A. Most of the radars are from the northern hemisphere. The geographic latitudes of the radars cover the range of 43-90 degrees - from mid- to polar latitudes and cover both hemispheres. For each radar we use the data over two years: one year of relatively low (2010, 2011, 2020, and 2021), and another year for relatively high solar activity (2014, 2023, and 2024). Solar activity is shown in Fig.2B by Wolf numbers. For any multi-channel radars except EKB and MAGW, only one of the channels was analyzed, that provides the best quality of elevation calibration and higher data amount.

The scattering signal distributions at radar ranges up to 350 km after the elevation calibration (usually interpreted as the scattering at altitudes of 90-100 km - meteor echo[16] and near-range echo at E-layer altitudes[27]) over the altitudes for each radar and year are shown in Fig.3. One can see from the figure that the elevation angle calibration is sufficiently good, both for years of low and high solar activity: the most probable scattering height corresponds to 100-110 km, well corresponding to the expected types of scattering. We interpret the signals scattered at altitudes of 150 km and above, for example by EKB radar, with a large proportion of signals from the back lobe of the antenna pattern[22, 6], which is not taken into account during further analysis.

3 Training the classifier

3.1 Selecting measurements for training

An important problem in massive automatic signal processing is the presence of signals coming not from the main lobe of the antenna pattern, but from the back lobe[22]. The problem of excluding such signals is quite complex. Their presence significantly distorts the operation of the algorithm, since it requires accurate raytracing and calculating trajectory parameters.

The selection of main-beam signals for training the model was carried out using signals with relatively low elevation angles [22]. The signals potentially arriving from the back lobe were detected by their high elevation angle exceeding the threshold level determined by the method [6] over the years of low and high solar activity. These threshold angles are determined based on the raytracing

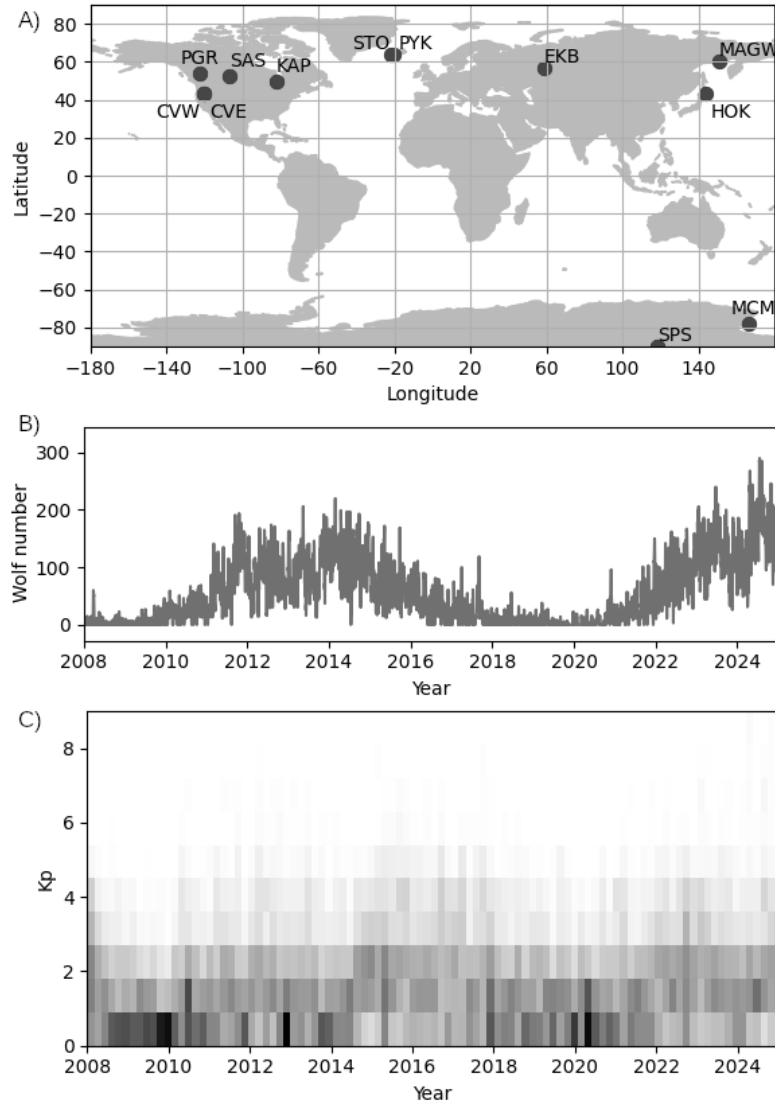


Fig. 2: A) Radars used in the paper; B) Wolf numbers for the period 2008-2024 [30]; C) Kp index distribution for 2008-2024 [14]

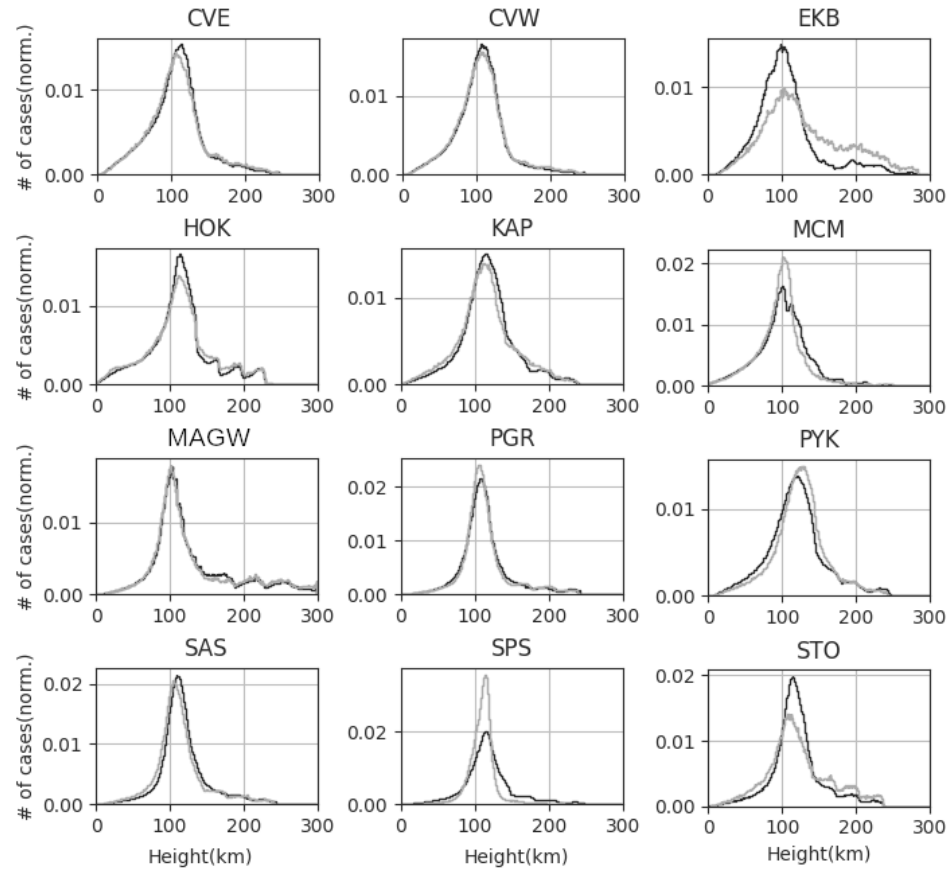


Fig. 3: Quality of radar elevation calibration: meteor scattering altitude distributions (range < 350 km, Doppler drift velocity < 50 m/s) for each radar over the year. Black line - year of low solar activity, gray - year of high solar activity.

Tab. 2: Threshold elevation angles for separating signals into main and back lobes (for years of low and high solar activity, and the maximum value between them), degrees

Radar	Low activity year	High activity year	Max threshold
CVE	28	33	33
CVW	28	35	35
EKB	29	43	43
HOK	29	35	35
KAP	21	33	33
MAGW	35	56	56
MCM	14	19	19
PGR	26	34	34
PYK	22	28	28
SAS	34	33	34
SPS	34	17	34
STO	27	31	31

results for measured signals - their altitudes in case of main beam should be within the range of ionospheric scattering altitudes (usually less than 350 km). Due to raytracing and actual radar measurements depends on geographical and geophysical factors, the threshold level depends on the radar and year. The calculated threshold levels for given radars and years are shown in the Table 2.

For further training of classifier, the median value of the threshold elevation angle over all maximums, 34 degrees, was chosen as the threshold elevation angle for all the radars. The average value differs little from it and is 34.6 degrees. Signals coming from elevation angles below the threshold were considered to come from the main lobe of the antenna pattern and were used for further analysis. The signals above thershold level were considered to come from the back lobe of the antenna pattern and were excluded from the model training and analysis. We have not used standard threshold level calculated from antenna spacing discussed in [22], because it works not good enough at ranges less 400km, and excludes too much actual main beam signals, especially meteor trail scattering used for the radar calibration.

3.2 Pre-training and estimating the number of latent classes in the data

The important problem of data analysis is determining the number of latent (hidden) classes in the data - how many different types of signals the radars actually observe. Traditionally, this number and types of signals are postulated by the researcher before building a classifier, and only the parameters of such a classifier are determined during training [26, 10, 28, 21, 20, 19]. This approach is typical for supervised learning. In the data-driven approach we propose that the number of hidden classes in the data is an unknown parameter to be found

from the measured data, and interpretation of these classes will be carried out after the classifier is trained and the data is separated into classes by it.

The search of a classifier for an unknown number of latent classes was carried out using the methodology described in details in [3]: at the first stage of training, the data of each experiment were clustered using the GM+BIC method (Gaussian Mixture as a clusterer, the optimal number of clusters corresponds to the minimum of Bayesian information criterion). The applicability of such a technique was discussed in detail in [3] - it gives a slightly overestimated number of clusters, but leads to well-interpretable results after the final training of the classifier. The data obtained with high spectral resolution (i.e. using 16-pulse sequences at EKB and MAGW radars instead of standard 7- or 8-pulse SuperDARN sequences) were augmented by spectral width (their spectral widths were increased accordingly). At the second stage of training, in accordance with [3], a very wide two-layer classifier neural network (300 and 140 neurons in the first and second network layers of Encoder, N,M respectively in Fig.1C) with absolute activation functions was trained. We train it at the data labeled at the first stage. At the third stage of training, according to the method [5], we find minimum sufficient number of neurons in the fully connected layers of the classifier network (i.e. optimize N,M in Fig.1C) to reach the forecast quality found at second stage. The minimum number of neurons in output classification layer (M in Fig.1C) corresponds to expected minimum number of latent classes in the data. At the fourth stage of training, the classifier was retrained again over the whole original data labeled by clusterer, but with the found minimum number of neurons in each layer of classifier.

The maximum number of clusters found by GM+BIC clusterer in each experiment was 52. The above first three stages of training were conducted and the minimum number of neurons in the classifier was found. An obvious initial assumption was the dependence of the number of latent classes in the measurements on the level of solar activity. Therefore, the classifier was initially trained in the three variants: by using only the data over the years of high solar activity, by using only the data over the years of low solar activity, and by using the data over all years.

For each of the models at stage 3 we calculated the minimum number of neurons in each classifier layer. The results are shown in Fig.4.

The figure shows that the number of neurons in the output layer (Layer 2, M in Fig.1C, the number of latent classes in the data) is almost the same for the years of low and high solar activity and for the full dataset (36, 37 and 35 classes, respectively). This suggests that the number of latent classes in the data is almost independent on the solar activity level, and almost the same number of different types of scattered signals is observed in all periods. It should be noted that this is in good agreement with the value of 35 classes found earlier for EKB and MAGW radar data over the year of low solar activity [3]. However, significant differences in the width of the first layer (Layer 1, N in Fig.1C) indicate that it is much more difficult to separate the data into classes at high solar activity than at low activity (more neurons in the hidden layer of the network are required to describe accurate boundaries between classes). This

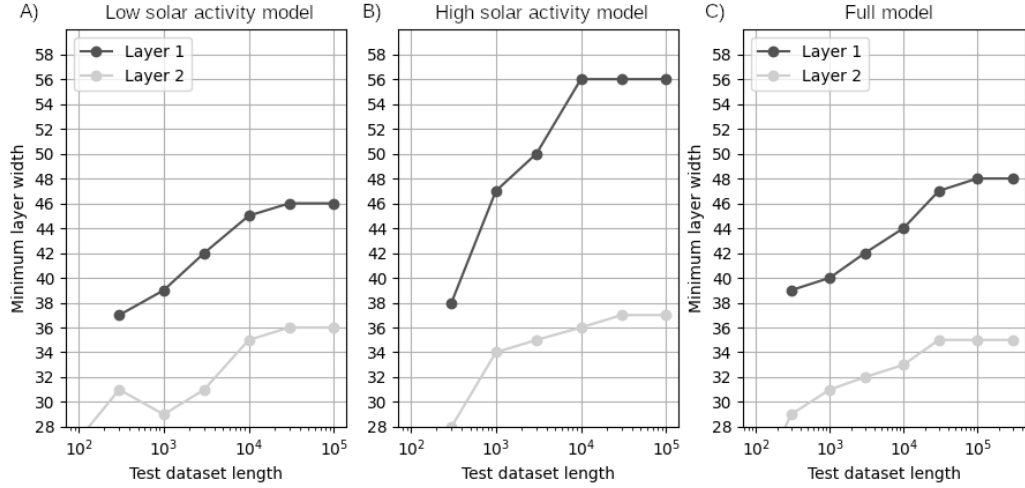


Fig. 4: Minimum number of neurons in different layers of the classifier neural network for years of low (A), high (B) solar activity, and for the whole data set (C) depending on the size of the subset used for the search. The size of Layer 2 is the expected number of latent classes in the data, Layer 1 is the hidden layer size of the classifier.

is also consistent with experimental observations - during high solar activity the signal interpretation is usually more difficult.

The figure shows that if the network is trained on the whole data set, the parameters will have approximately the average value between the years of low and high solar activity, which especially affects the first layer, the size of which corresponds to the complexity of classes separation. The number of latent classes is practically the same.

4 The final classifier

4.1 Choosing the optimal model

It should be noted that a slight increase in the number of neurons in the hidden layers of the neural network does not worsen the quality of the approximation, but leads to an increase in the number of model parameters. Therefore, in order to ensure good quality of approximation in all solar activity conditions for a network trained at all data (low and high solar activity), it is convenient to choose 56 neurons in the first layer and 37 neurons in the second layer, according to the years of high solar activity. It should be noted that the classification problem is non-convex (has more than one local minimum), so the optimal model depends on the initial state used to train the model (i.e. on pretrain stage).

To find the optimal model and the optimal number of classes in the data, the final classifier was trained in the following five variants:

- Model L (Low activity): pre-training (estimate of the initial approximation of the neural network coefficients) at a small data set extracted from the years of low solar activity, followed by full training at the entire data set of low solar activity. The optimal classifier size corresponds to the years of low solar activity - 36 classes and 46 neurons in the hidden layer (Fig.4A);
- Model H (High activity): pre-training at a small data set extracted from years of high solar activity, followed by full training at the entire data set of high solar activity. The optimal size corresponds to the years of high solar activity - 37 classes and 56 neurons in the hidden layer (Fig.4B);
- Full model A: pretraining at the data set extracted from the full data set, followed by full training at whole data set. The optimal size corresponds to the full dataset - 35 classes and 48 neurons in the hidden layer (Fig.4C);
- Full model B: pretraining at the small dataset extracted from the years of high solar activity followed by full training at whole data set. The optimal size corresponds to the years of high solar activity - 37 classes and 56 neurons in the hidden layer (Fig.4B);
- Full model C: pretraining at the dataset extracted from the whole dataset, followed by full training at whole data set. The optimal size corresponds to the high solar activity years - 37 classes and 56 neurons in the hidden layer (Fig.4B).

For all the models, training was performed by cross-validation over three folds (three almost independently trained variants of each model were obtained). Pretraining allows choosing a good initial approximation and includes, at the first, training the model (encoder + decoder) at 1000 random experiments from the pretraining dataset, and at the second, training the decoder at the entire training dataset without additional training of the encoder. Pretraining is made in the following way to avoid permutation of class numbers (this is an effect typical for hidden layers of neural networks): during pretraining only one variant has randomly initited network coefficients before training during cross-validation, the other two variants use its trained coefficients as their initial approximation before pretraining. The results for 5 network variants for 3 cross-validated versions of each model are shown in the Table 3. Quality metric caluclation (area under the precision-recall curve, AUC-RP, informative for complex data with strong class imbalance) was calculated for each of the models at the corresponding validation part of the dataset; at the test data set, the results were close to them with error about 10^{-3} .

Although statistically AUC-RP is approximately the same in all five cases (in terms of its confidence interval), the last network variant looks more acceptable - although it is slightly worse than the model trained on years of high solar activity (model H), but its quality was calculated at the whole dataset and it was trained at the whole dataset. It becomes clear when comapring Full model C with Full model B (it is model H but trained at the whole dataset): Full model B looks slightly worse than the Full model C.

Therefore, bellow by the Full model we will mean the Full model C: with sizes determined by years of high solar activity, but pre-trained and trained at

Tab. 3: Results of training possible classifier models on three folds

Train procedure				AUC-RP			
Model	Dim	Pretrain	Train/Test	@1	@2	@3	Mean
L	36x46	low activity	low activity	0.9048	0.9080	0.9031	0.9053
H	37x56	high activity	high activity	0.9040	0.9122	0.9067	0.9076
Full A	35x48	all	all	0.8945	0.9082	0.9062	0.9030
Full B	37x56	high activity	all	0.8981	0.9087	0.9064	0.9044
Full C	37x56	all	all	0.9044	0.9127	0.9038	0.9069

the whole data set. Qualitatively, such a model allows separating the signal classes both during years of high and low solar activity sufficiently well.

It should be noted that any version of the model trained at one of the folds could be used for the classification, as well as the ensemble model - a model that predicts a class only if all three model cross-validation variants predict the same class. In the subsequent detailed analysis more accurate ensemble version was used.

4.2 Identifying well-distinguished classes

An important issue is finding well- and poorly distinguishable classes from these 37 detected classes. This corresponds to the following statement of the problem: which classes are objectively separated well by any good classification model, and which classes can be detected only by some classification models? A possible answer to this question can be found by comparing the predictions of the three models (L, H, and Full C models). If we have signal classes that are unambiguously classified by any of these models, then these classes are well distinguishable in the data. The remaining detectable classes are subjective and depend significantly on the model used or from the researcher.

To find well distinguishable classes, we compare how the three models (L, H, and Full C) classify our data. Let us compare the results between any two models. To do this, let us determine how likely each class identified by some model (Model 1) is identified by another model (Model 2). We can construct a confusion matrix - the number of correspondences between different signal classes identified by these different models. The results for the three possible pairs of the models are shown in Fig.5A-C. It is found that the Rand index (the percent of pairs of identically clustered points) is about 91% and higher, which indicates that, in average, 91% of signal pairs are combined into classes by all these models in the same way. The Adjusted Rand index (the excess of the percent of identically clustered pairs of signals compared to random clustering) is also acceptable, although numerically lower (but at least 35%).

To find the well-separated signal classes between which the most probable one-to-one correspondence can be established, we perform the following procedure:

- using the confusion matrix for each class of Model 1, we find the most

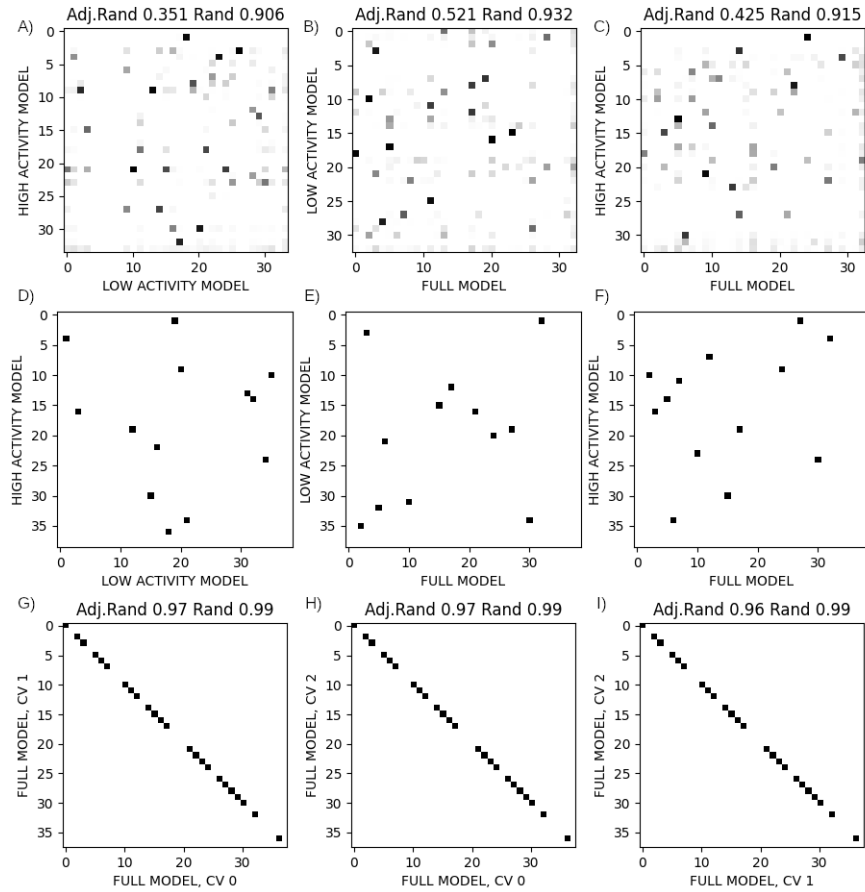


Fig. 5: Data classification comparison for three models: correspondence between classes defined by different algorithms - L, H, and Full. A-C) confusion matrices for non-zero classes, D-F) matrices of best one-to-one correspondence between classes detected by two models; G-I) matrix of best on-to-one correspondence between variants of the Full model in the ensemble (during cross-validation). The title of the plot indicates the value of the Rand index and the Adjusted Rand index.

probable class of Model 2.

- using the confusion matrix for each class of Model 2, we find the most probable class of Model 1.
- if the correspondence of classes between the models is the same in both cases, we will consider the two found classes to be the most probable one-to-one correspondent, or well-distinguished.

The matrices of most likely one-to-one class correspondence between models are shown in Fig.5D-F.

The figure shows that the data we analyze contains 12 well-distinguished classes during years of low solar activity and 14 - during years of high solar activity. We will discuss the interpretation of the detected classes below. The remaining classes are subjective ones because could depend on the model used.

4.3 Interpretation of classes

Unlike most standard approaches to classifying coherent scatter radar data, in this data-driven approach we first classify the signals and then interpret classes. To interpret the data, by analogy with [8, 3], statistics of various parameters for signals assigned to each signal class are calculated. The parameters chosen are: the scattering height according to the IRI ray-tracing results (Hiri), the signal hops (Mode, the number of scattering/reflections from the underlying layers), the radar range to the scatterer (Range), the Doppler velocity measured (Vd), the spectral width of the received signal in Doppler velocity units (Wl), the cosine of the aspect angle of the radio wave vector with the Earth's magnetic field at the calculated scattering point ($\cos(k, B)$), and the elevation angle of the trajectory at the calculated scattering point ($\sin(k, xy)$). In Fig.6 for each class the 95% confidence interval for each of these parameters is shown. From the figure it is possible to make a qualitative interpretation the main groups of classes: the signals, scattered from the earth's surface; the signals, scattered from the ionosphere; and the signals, which are difficult to interpret.

The group of classes of the signals scattered from the earth's surface (marked by light gray color in Fig.6) includes 4 classes: 5, 11, 12, 15. The main feature of these signals is their low scattering height (below 100km), relatively low drift velocity and spectral width. Additional information about the possible nature of scattering can be provided by the mode - the number of reflections from the underlying surface.

The group of signal classes with complicated interpretation (marked by black color in Fig.6) includes 9 classes: 6, 14, 16, 23, 24, 26, 27, 28, 32. Their interpretation is complicated due to their very high altitudes, unusual for the ionospheric scatter, and a large spread of velocities or spectral widths. In the future, these classes require more careful analysis and interpretation.

The group of classes of signals scattered from the ionosphere includes all other signals (marked by gray color in Fig.6). These are 12 classes: 0, 2, 3, 7, 10, 17, 21, 22, 29, 30, 31, 36.

It should be noted that 12 classes are practically not observed in the experiments (classes 1, 4, 8, 9, 13, 18-20, 25, 33-35), which is due either they are very

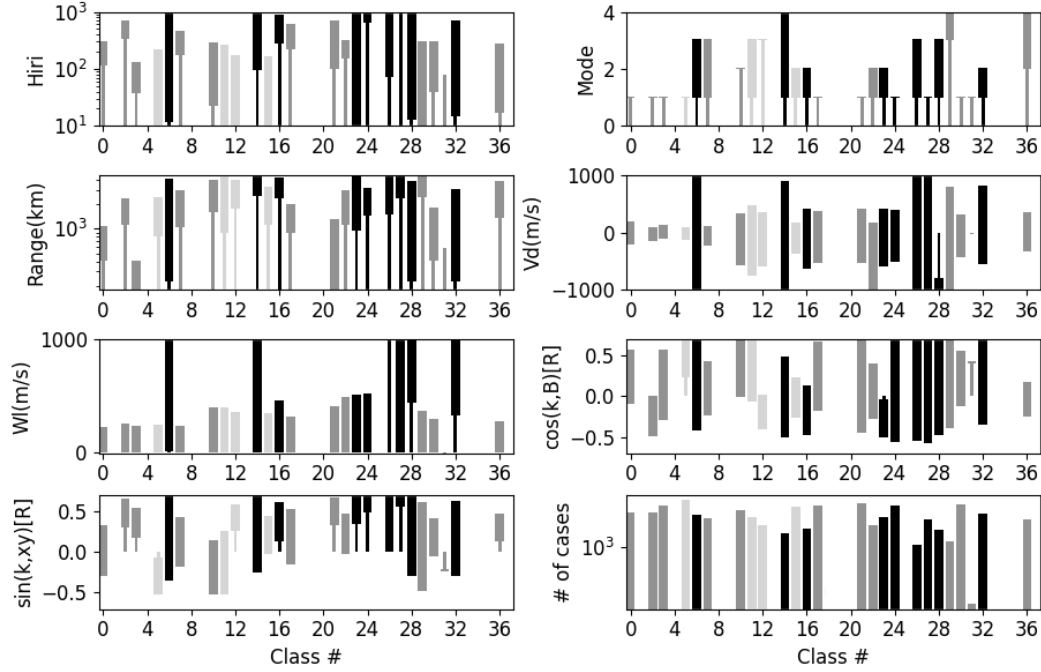


Fig. 6: Confidence intervals (95%) of various signal parameters for each class. Black - uninterpreted signal types, gray - ionospheric scatter types, light gray - groundscatter types.

rare, or that they are mathematically "balancing" classes necessary to provide the best fit between the classification and clustering results at the training stage (the clustering could differ from actual physical classes separation and therefore is not optimal). This could be also a sign that the absolute activation function we used is not optimal, and replacing it with another activation function may help to simplify the classifier and reduce the number of latent classes without losing the classification quality.

According to the analysis, there are total 25 frequently observed classes in the data, and 16 of them are interpretable classes, which are shown in Table 4 together with another, poorly interpretable classes. The 14 well-distinguished classes(Fig.5D-F) are highlighted in bold.

Of these classes, 8 cases (2, 3, 5, 10, 15, 17, 21, 30) correspond to scattering at ionospheric altitudes and below with velocities and spectral widths less than 1 km/s, so they can be interpreted from a radiophysical point of view. At high solar activity level, there are two more classes exist, which are difficult to distinguish at a low level of solar activity. These are classes 7 and 12. We can interpret the 10 classes from a physical point of view as follows:

- Groundscatter at 1st hop (class 5);

Tab. 4: Preliminary interpretation of some classes. Classes in bold are well-distinguished classes according to the models L, H, and Full.

#Full	Interpretation	Comments
0	E/F 0.5 hop	low V,W
2	F 0.5 hop	low V,W
3	Meteor/near-range E 0.5 hop	low V,W
5	GS, 1hop	low V,W
6	Uninterpreted	too high H,V,W
7	F, 1-3hop	low V,W, aspect
10	E, 1.5hop	intermediate V,W
11	GS, 1-3hop	high V, intermediate W
12	GS, 3 hop	high V, intermediate W
15	GS, 2 hop	low V,W
17	F 0.5 hop	intermediate V, low W
21	near-range F 0.5hop	intermediate V, low W
22	E/F 0.5hop	high V,W, aspect
24	Uninterpreted	too high H
27	Uninterpreted	too high H,V,W
29	E, 3.5hop	high V, intermediate W
30	E/F 0.5hop	intermediate V, low W
31	Rare class	too few observations
32	Uninterpreted class	too high H
36	E/F 2-4hop	low V,W, aspect

- Groundscatter at 2nd hop (class 15);
- Groundscatter at 3rd hop (class 12, clearly distinguished during high solar activity);
- Meteor/near-range E scatter at 0.5 hop (class 3);
- near-range F-layer scatter at 0.5 hop (class 21);
- E or F layer scatter at 0.5 hop (class 30).
- F layer scatter at 0.5 hop with low V and W (class 2);
- F layer scatter at 0.5 hop, with intermediate V and low W (class 17);
- E layer scatter at 1.5 hop with intermediate V and W (class 10);
- F layer scatter at hops 1-3 with low V and W (class 7, clearly distinguished during high solar activity);

Four classes (6,24,27,32) are poorly interpretable.

4.4 Importance of different parameters for classification

An important issue discussed today is the question of which parameters need to be taken into account for accurate classification of the radar data, in particular the need to take into account the elevation angle[24]. Within the framework of the proposed model, this task is reduced to the task well-known in machine learning - Feature Importance: determining the parameters that significantly affect the result of the model. One of the feature importance algorithms was used in a similar task in [19].

One of the universal methods that allows this to be done is the permutation feature importance method [11, 17], in which the importance of an input parameter for a forecast is judged by the change of the forecast quality when the values of this parameter in the data set are randomly permuted.

Fig.7 shows the importance of the different input parameters for identifying the different classes according to this method described in [3], with a higher value corresponding to more important parameter. The importance of the final classification is also shown (column 'R'). The results are shown for each network variant obtained during cross-validation train process. Empty cells correspond to minimally important parameters.

From Fig.7 it is evident that the most important parameters for classification are: the elevation angle of the radio wave propagation trajectory at the scattering point and at 3/4 of the path length, the ray-traced scattering height, and also nearly equally the angle with the Earth's magnetic field at the scattering point and the elevation angle in the middle of the signal propagation trajectory. The least important parameters are the signal propagation mode and the spectral width of the received signal. Thus, the most important parameters for

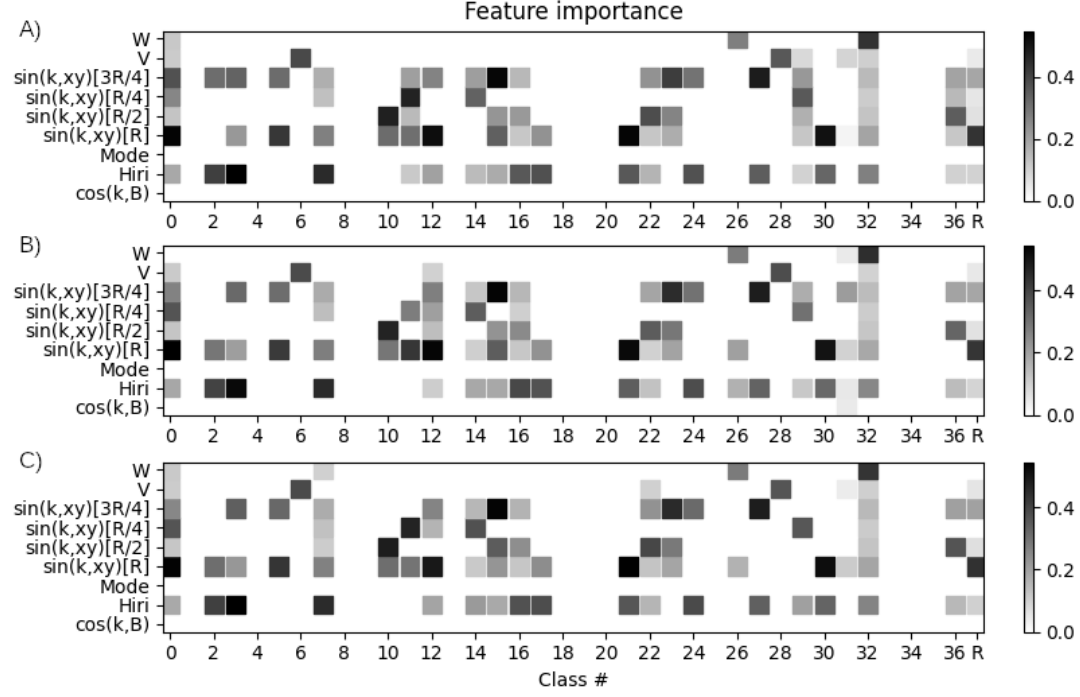


Fig. 7: Feature importance for different network variants trained on different cross-validation folds (A,B,C) and for different classes. Column R is the importance for the whole classification.

classifying scattered signals are the shape of the radio signal propagation trajectory at its last half and the scattering height. These parameters cannot be measured directly by the radar and require simulation of the radio wave propagation process. To do this, it is necessary to know the sounding frequency, the three-dimensional antenna pattern, the radiowave elevation angle and azimuth, and the three-dimensional structure of the ionospheric refractive index. It is obvious that in complex situations, when the propagation trajectory is difficult to predict (there are no reliable measurements of the elevation angle of the received radio wave or there is no sufficiently accurate model of the ionosphere), this method will produce significant errors. This explains the wide use of simpler classification methods based on velocity and spectral width [26, 10] at high-latitude radars. This could be seen from Fig.7: the spectral width is important for classification only for 0th,7th,26th,31st,32nd classes - the most difficult classes for interpretation from raytracing point of view (Fig.5F, Fig.6, Table 4).

For the radars with calibrated elevation angle measurements, the simulation of the radio wave propagation trajectory with IRI model shows that the classification method we developed can be successfully applied.

Unexpected results are weak dependence of the classifier quality on the spectral width and on the trajectory angle with the magnetic field. The first result can be explained by the presence of trajectory information, which provide a better estimate of the scattering heights than taking into account the spectral width. The second result can be caused by errors in the ionospheric model and trajectory calculations, which significantly complicate the verification of the conditions of aspect sensitivity with the magnetic field.

The final classifier model thus has the following form. The output (logit) of the model m for each of the classes k is:

$$y_{km} = \left| \sum_{j=1}^{56} C_{kjm} \left(\left| \sum_{i=1}^9 A_{ijm} x_i + B_{jm} \right| \right) + D_{km} \right| \quad (1)$$

$m=1..3$ is the model identifier in the ensemble, $k=0..36$ is the class number, and x_i are nine input parameters of the model obtained from the measurements and propagation trajectory simulation. Matrices A , B , C , D are model parameters found during model training.

The maximum probable class K_m for a given signal determined by model m is the class corresponding to the maximum logit y_{km} :

$$K_m = \operatorname{argmax}_{k \in [0, 36]} (y_{km}) \quad (2)$$

The signal class should be identified similarly by all three models in the ensemble (or the signal is identified as a new class 37, corresponding to uncertainly classified signals):

$$K = \begin{cases} K_0, & \text{if } K_0 = K_1 = K_2 \\ \text{else } 37 \end{cases} \quad (3)$$

Fig.5G-I shows a comparison of the signal identification by all three network variants in terms of confusion matrix, used before. It is evident that in most cases these 3 models provide almost identical classification (Rand index > 0.99 , Adjusted Rand index > 0.96). This means that, if necessary, to simplify or speed up the classification, it is possible to use only one of the three models trained in the cross-validation process, for example y_{k0} (2), without using ensemble processing (3). Thus, the sufficient model has the form (1,2) and has 2669 coefficients.

To simplify the model one could take into account only 25 of 37 classes actually observed in the experiment (Fig.6H), rare classes can be ignored in the calculations and the number of coefficients in the model can be reduced down to 1985.

The final trained ensemble version of the classifier model is available at https://github.com/berng/SECIRA_SD_Classifier/.

5 Discussion

The dependence of different scattering types on geographical location and geo-physical conditions is well known experimental fact. Let us estimate the dependence of observation occurrence of different classes at different radars depending on geophysical conditions. To do this, based on the data of each radar (the test part of the dataset that was not used to train the classifier), we calculate the frequency (probability) of observations of each class. Calculating the obserav-
tion frequency and, in general, a kind of normalizing the number of observations is necessary due to radars can change their operating regimes, scanning regimes and temporal resolution. Therefore the absolute number of observations of a signal class would not be an indicative characteristic.

Fig.8A-B shows the probability of observing different classes by different radars depending on the level of solar activity and the radar latitude. It is evident from the figure that this dependence is significant. One can see the decrease of the occurrence frequency of class 3 signals (meteor trail scattering and near-range echo from the lower layers of the ionosphere) and classes 21, 24, 30 (near-range 0.5 hop scatter from F-layer; Uninterpreted class; 0.5 hop scatter from E/F layers with medium V and low W, respectively). Apparently, the decrease of the occurence frequency of class 3 may be unjustified in most cases (meteor scattering should not depend strongly on the level of solar activity, since it is more likely to be associated with astronomical features of meteor showers than with solar activity, and the radiowave absorption in the lower part of the ionosphere is relatively small due to high elevation angles to the meteor trails at short ranges). Therefore, it makes sense to consider not the occurrence frequency of different echo types at each radar, but their relation to the class with a nearly regular occurrence, for example with meteor trail echo at the corresponding radar.

Fig.8C-D shows the number of observations of different classes relative to the number of observations of class 3 at the radar depending on the solar activity level and the radar geographical latitude. These figures allow a fairly convincing interpretation of the results from a physical point of view.

It is obvious from the figure that the strongest effect is observed in the increase in the class 5 signals - scattering from the earth's surface at the first hop (1st hop groundscatter). This is easily explained by the growth of the electron density during years of high solar activity, and as a consequence - an increase of the signals number propagating with reflection from the ionosphere, including scattered from the earth's surface.

The increase of number of signals of the ionospheric scattering classes (7,10,17,22,36), scattering from the earth's surface at the second hop (15) and uninterpreted signals (6,23) also confirms the well-known experimental fact that under high solar activity conditions the number of scattered signals of various types increases: the number of signals scattered from the ionosphere increases with the growth of ionospheric small-scale irregularities, the number of signals scattered at the second hop from the earth's surface increases with electron density growth, and the number of uninterpreted signals increase due to the growth of the amplitude

of various large-scale ionospheric irregularities, disturbing raytracing results.

A special group of radars is polar radars in south hemisphere - MCM and SPS. They observe mainly only 7 classes of the signals. These are 4 classes associated with scattering in the ionosphere: 3 (meteor trail scattering), 17 (0.5hop F-layer scattering), 21 (0.5 hop near-range F-layer scattering), 30 (0.5hop E/F-layer scattering), and three uninterpreted classes: 6, 24, 32. These radars have not observed any groundscatter signals. This is related with the ice covering nearby territory and preventing reflection back at off-perpendicular angles [25].

Also interesting the group of three lowest-latitude radars: CVE, CVW, and HOK. At high levels of solar activity they observe signal classes that are less frequently observed by other radars - 11 and 12. The classes are unusual types of scattering from the earth's surface - with high velocities (class 11) and with three hops (class 12). The appearance of class 12 can be explained by the following. For relatively low-latitude radars, even a very long propagation trajectory can lie below the polar oval - an area of strong absorption, so the signals with a high number of hops are not affected by strong attenuation, in opposite to higher latitude radars. The appearance of class 11 has not yet been explained, and may be associated, among other things, with their incorrect interpretation as scattering from the earth's surface (for example, this could be scattering from the E-layer at a 1.5 hop).

The dependence of the occurrences of different classes normalized to observations of class 3 on geomagnetic activity is shown in Fig.9. It is evident from the figure that this dependence is significant. Fig.9 shows that occurrence of most classes, especially class 5 (1st hop groundscatter) decrease with K_p growth. This is well known fact (radio blackout), associated with the growth of ionospheric absorption and the decrease of electron density during geomagnetic disturbances.

Also, Fig.9 shows a significant increase of some signal classes occurrence at lower-latitude radars with increasing K_p : groundscatter of the 1st and 2nd hops (classes 5,15), scattering from the F-layer of the 1st-3rd hop (class 7), as well as an increase of occurrence of uninterpreted classes (6, 23, 24, 27, 28, 32). This is also explainable - during significant geomagnetic disturbances, a radio blackout is observed at most high-latitude radars, and only the lowest-latitude ones observe scattered signals, including scattering in the F-layer, typical for geomagnetic disturbances. During geomagnetic disturbances it is harder to use IRI model for describing actual ionosphere, so more signals become uninterpretable.

Fig.10 shows the occurrence of different classes at different radars during high solar activity years at test data set, not used for training the classifier. One can see that found classes are correspondant between different radars and have explainable range-time dependence. Time offsets of same classes at different radars corresponds to local solar time difference at different longitudes.

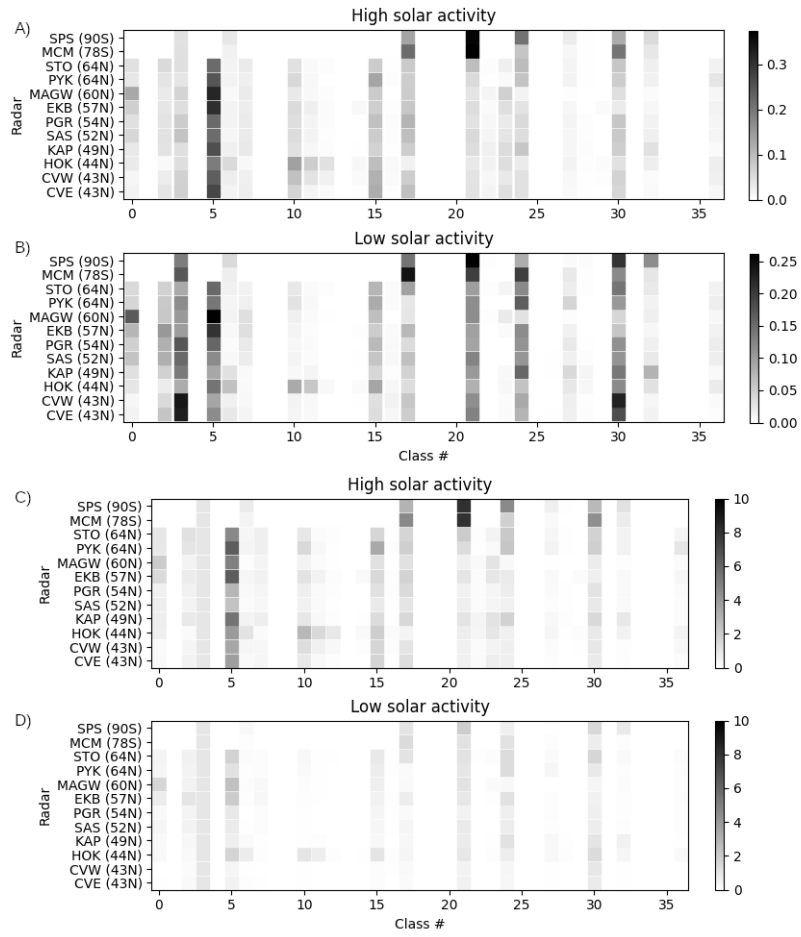


Fig. 8: Occurrence of different classes depending on the radar latitude and solar activity level. A,B) - normalized to the total number of observations at each radar, C,D) - normalized to the number of observations of class 3 at each radar.

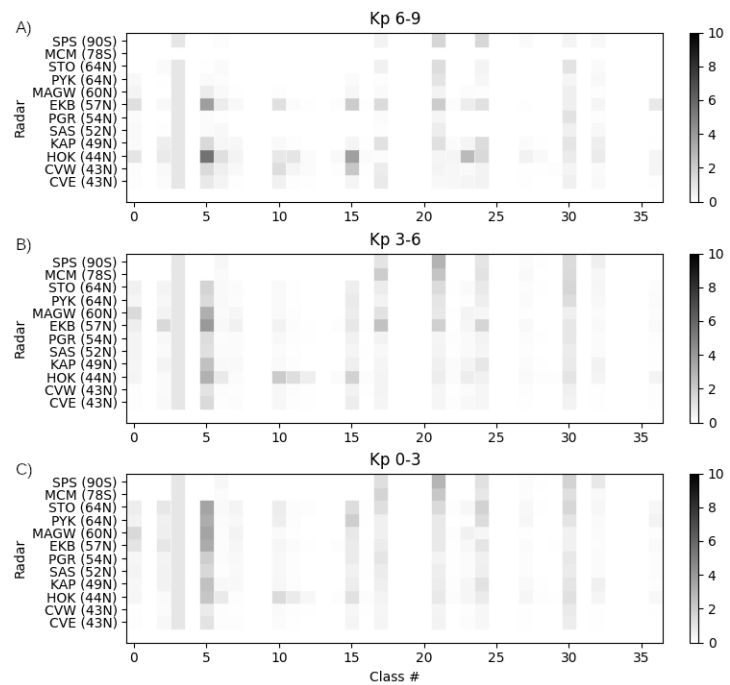


Fig. 9: Occurrence of different classes on the radars depending on the radar latitude and the level of geomagnetic activity, normalized to the number of observations of class 3 (meteors/E-layer near-range echo) at each radar. There were no data on the MCM radar during the studied periods with Kp 6-9.

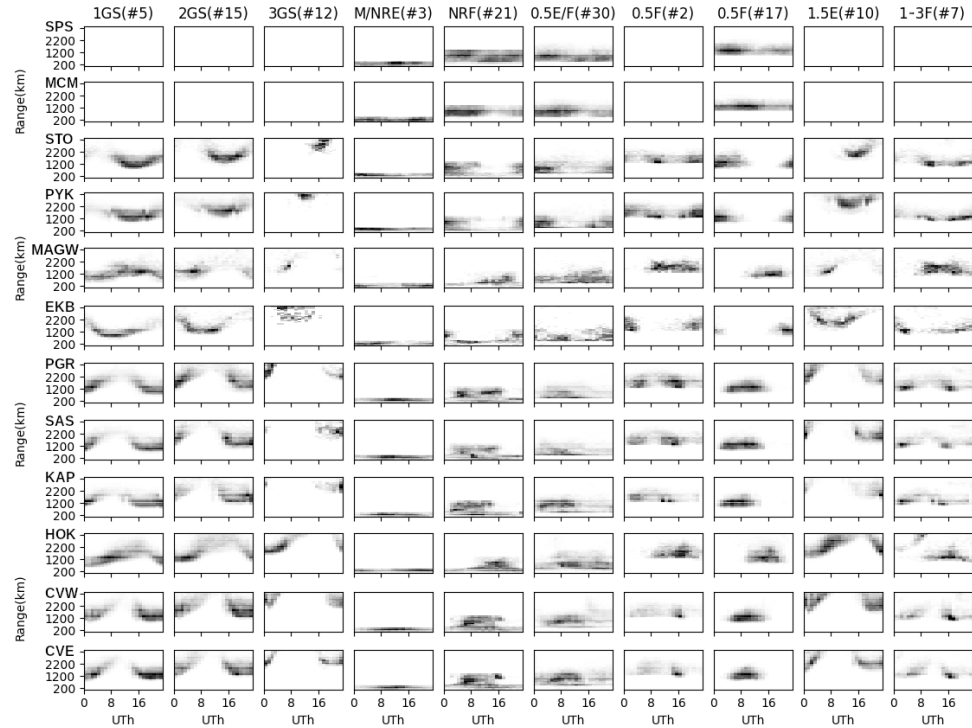


Fig. 10: Range-time occurrence of different classes at different radars during high solar activity years (the data not used for training).

6 Conclusion

The paper presents a method for automatic constructing a classifier of processed data obtained by SuperDARN and SECIRA radars without making additional assumptions. Method is based only on the radar data, the results of automatic radiowave tracing in the IRI-2020 model ionosphere, and mathematical criteria for estimating the quality of the models.

The final classifier is an ensemble model consisting of three network variants trained on three random partitions of the available dataset (12 radars of the SuperDARN and SECIRA networks, 1 year of low and 1 year of high solar activity for each radar) using the wrapped classifier method, when clustering of the dataset is used to label it [8]. The number of detected classes in the data is 37, of which 25 are frequently observed in the experiments, which is close to the results obtained for EKB and MAGW radars in [3]. The model has the form (1-3). The number of parameters for each network is 2669, which is significantly simpler than the models [8, 2] and close to the model [3]. When classifying radar data, the model requires both calculated parameters of radio wave propagation in the model ionosphere and parameters directly measured by the radar. When calculating the elevation angle, the radars are calibrated using scattering on meteor trails, assuming their 104km scattering altitude.

The analysis allowed us to identify 14 classes that were well-identified by training different classification models. We can interpret 10 classes of them from a physical point of view as 3 groundscatter classes and 7 ionospheric scatter classes. The remaining classes depend on the variant of the dataset used for training, or are uninterpreted due to problems in calculating the radiowave trajectory. Therefore in different cases (different models or researchers) they can be grouped and interpreted differently, so require more detailed study. It should be noted that the propagation model we use does not distinguish between hops from the earth's surface and from underlying layers, so when interpreting multi-hop propagation, the hops can be associated not only with scattering from the earth's surface, but also with interlayer waveguide propagation. Thus, in any geophysical data analysis, it is looks useful to first pay attention to these 10 classes, since they will be most reliably distinguished by different classification models or human researchers.

The analysis showed that from the parameters used for class identification, the most important parameters are the calculated shape of the signal propagation trajectory at its second half, the scattering height and the measured Doppler velocity.

The average dynamics of observation of classes and their dependence on the geographical latitude of radars at different levels of solar and geomagnetic activity looks explainable and do not contradict known patterns and mechanisms.

The final trained classifier model is available at https://github.com/berng/SECIRA_SD_Classifier/

Acknowledgments

The work of OB and IL was supported by a grant from the Russian Science Foundation #24-22-00436, <https://rsrf.ru/project/24-22-00436/>.

The authors acknowledge the use of SuperDARN data. SuperDARN is a collection of radars funded by national scientific funding agencies of Australia, Canada, China, France, Italy, Japan, Norway, South Africa, United Kingdom and the United States of America. SuperDARN data is available at <https://www.frdr-dfdr.ca/repo/search?query=superdarn>. SECIRA data is available at http://sdrus.iszf.irk.ru/ekb/page_example/simple.

References

- [1] J. D. Banfield and A. E. Raftery. Model-based gaussian and non-gaussian clustering. *Biometrics*, 49(3):803–821, 1993.
- [2] O. Berngardt. The first comparative analysis of meteor echo and sporadic scattering identified by a self-learned neural network in EKB and MAGW ISTP SB RAS radar data. *Solar-Terrestrial Physics*, 8(4):63–72, 2022.
- [3] O. Berngardt. Data-driven approach to mid-latitude coherent scatter radar data classification (in russian). *Solar-Terrestrial Physics*, 11:22–44, 2025.
- [4] O. Berngardt, V. Kurkin, D. Kushnarev, K. Grkovich, R. Fedorov, A. Orlov, and V. Harchenko. ISTP SB RAS decameter radars. *Solar-Terrestrial Physics*, 6(2):63–73, 2020.
- [5] O. I. Berngardt. Minimum number of neurons in fully connected layers of a given neural network (the first approximation). *arXiv e-prints*, page arXiv:2405.14147, 2024.
- [6] O. I. Berngardt and R. Fedorov. Signals scattered in the main and back lobes of antenna pattern of ISTP SB RAS coherent scatter radars. *Radio-physics and Quantum Electronics*, in press, 2025.
- [7] O. I. Berngardt, R. R. Fedorov, P. Ponomarenko, and K. V. Grkovich. Interferometric calibration and the first elevation observations at EKB ISTP SB RAS radar at 10-12 MHz. *Polar Science*, 28:100628, 2021.
- [8] O. I. Berngardt, O. A. Kusonsky, A. I. Poddelsky, and A. V. Oinats. Self-trained artificial neural network for physical classification of ionospheric radar data. *Advances in Space Research*, 70(10):2905–2919, 2022.
- [9] D. Bilitza, M. Pezzopane, V. Truhlik, D. Altadill, B. W. Reinisch, and A. Pignalberi. The International Reference Ionosphere Model: A Review and Description of an Ionospheric Benchmark. *Reviews of Geophysics*, 60(4):e2022RG000792, 2022.

- [10] G. T. Blanchard, S. Sundein, and K. B. Baker. Probabilistic identification of high-frequency radar backscatter from the ground and ionosphere based on spectral characteristics. *Radio Science*, 44(5), 2009.
- [11] L. Breiman. *Machine Learning*, 45(1):5–32, 2001.
- [12] G. Chisham and M. P. Freeman. A reassessment of SuperDARN meteor echoes from the upper mesosphere and lower thermosphere. *Journal of Atmospheric and Solar-Terrestrial Physics*, 102:207–221, 2013.
- [13] G. Chisham, M. Lester, S. Milan, M. Freeman, W. Bristow, K. McWilliams, J. Ruohoniemi, T. Yeoman, P. Dyson, R. Greenwald, T. Kikuchi, M. Pinnoch, J. Rash, N. Sato, G. Sofko, J.-P. Villain, and A. Walker. A decade of the super dual auroral radar network (superdarn): scientific achievements, new techniques and future directions. *Surv Geophys*, (28):33–109, 2007.
- [14] GFZ Helmholtz Centre for Geosciences. Kp index, <https://kp.gfz.de/>, 2025.
- [15] R. Greenwald, K. B. Baker, J. R. Dudeney, M. Pinnoch, T. Jones, E. Thomas, J.-P. Villain, J. C. Cerisier, C. Senior, C. Hanuise, R. D. Hunsucker, G. Sofko, J. Koehler, E. Nielsen, R. Pellinen, A. Walker, N. Sato, and H. Yamagishi. Darn/superdarn: A global view of the dynamics of high-latitude convection. *Space Science Reviews*, 71:761–796, 1995.
- [16] G. E. Hall, J. W. MacDougall, D. R. Moorcroft, J.-P. St.-Maurice, A. H. Manson, and C. E. Meek. Super Dual Auroral Radar Network observations of meteor echoes. *Journal of Geophysical Research: Space Physics*, 102(A7):14603–14614, 1997.
- [17] X. Huang, D. Kroening, W. Ruan, J. Sharp, Y. Sun, E. Thamo, M. Wu, and X. Yi. A survey of safety and trustworthiness of deep neural networks: Verification, testing, adversarial attack and defence, and interpretability. *Computer Science Review*, 37:100270, 2020.
- [18] A. Kolmogorov. On the representation of continuous functions of many variables by superposition of continuous functions of one variable and addition. *Dokl. Akad. Nauk SSSR*, pages 953–956, 1957.
- [19] X. Kong, E. Liu, S. Shi, and F. Chen. The implementation of deep clustering for SuperDARN backscatter echoes. *Advances in Space Research*, 74(1):243–254, 2024.
- [20] B. S. R. Kunduri, J. B. H. Baker, J. M. Ruohoniemi, E. G. Thomas, and S. G. Shepherd. An Examination of SuperDARN Backscatter Modes Using Machine Learning Guided by Ray-Tracing. *Space Weather*, 20(9):e2022SW003130, 2022.
- [21] I. A. Lavygin, O. I. Berngardt, V. P. Lebedev, and K. V. Grkovich. Identifying ground scatter and ionospheric scatter signals by using their fine structure at ekaterinburg decametre coherent radar. *IET Radar, Sonar & Navigation*, 2019.

- [22] S. E. Milan, T. B. Jones, T. R. Robinson, E. C. Thomas, and T. K. Yeoman. Interferometric evidence for the observation of ground backscatter originating behind the CUTLASS coherent HF radars. *Annales Geophysicae*, 15(1):29–39, 1997.
- [23] N. Nishitani, J. M. Ruohoniemi, M. Lester, J. B. H. Baker, A. V. Koustov, S. G. Shepherd, G. Chisham, T. Hori, E. G. Thomas, R. A. Makarevich, A. Marchaudon, P. Ponomarenko, J. A. Wild, S. E. Milan, W. A. Bristow, J. Devlin, E. Miller, R. A. Greenwald, T. Ogawa, and T. Kikuchi. Review of the accomplishments of mid-latitude super dual auroral radar network (SuperDARN) HF radars. *Progress in Earth and Planetary Science*, 6(1), 2019.
- [24] P. Ponomarenko and K. A. McWilliams. Climatology of HF Propagation Characteristics at Very High Latitudes From SuperDARN Observations. *Radio Science*, 58(5):e2023RS007657, 2023.
- [25] P. V. Ponomarenko, J.-P. St. Maurice, G. C. Hussey, and A. V. Koustov. HF ground scatter from the polar cap: Ionospheric propagation and ground surface effects. *Journal of Geophysical Research: Space Physics*, 115(A10), 2010.
- [26] P. V. Ponomarenko, C. L. Waters, and F. W. Menk. Factors determining spectral width of HF echoes from high latitudes. *Annales Geophysicae*, 25(3):675–687, 2007.
- [27] V. Ponomarenko, Pavlo, B. Iserhienrhien, and J.-P. St.-Maurice. Morphology and possible origins of near-range oblique hf backscatter at high and midlatitudes. *Radio Science*, 51(6):718–730, 2016.
- [28] A. J. Ribeiro, J. M. Ruohoniemi, J. B. H. Baker, L. B. N. Clausen, S. de Larquier, and R. A. Greenwald. A new approach for identifying ionospheric backscatter in midlatitude SuperDARN HF radar observations. *Radio Science*, 46(4), 2011.
- [29] A. J. Ribeiro, J. M. Ruohoniemi, P. V. Ponomarenko, L. B. N. Clausen, J. B. H. Baker, R. A. Greenwald, K. Oksavik, and S. de Larquier. A comparison of SuperDARN ACF fitting methods. *Radio Science*, 48(3):274–282, 2013.
- [30] Royal Observatory of Belgium. Sunspot index, <https://www.sidc.be/silso/datafiles>, 2025.
- [31] D. E. Rumelhart, G. E. Hinton, and R. J. Williams. Learning Internal Representations by Error Propagation. In *Parallel Distributed Processing, Volume 1: Explorations in the Microstructure of Cognition: Foundations*. The MIT Press, 1986.
- [32] G. Schwarz. Estimating the Dimension of a Model. *The Annals of Statistics*, 6(2):461 – 464, 1978.

- [33] E. Thébault, C. C. Finlay, C. D. Beggan, P. Alken, J. Aubert, O. Barrois, F. Bertrand, T. Bondar, A. Boness, L. Brocco, E. Canet, A. Chambodut, A. Chulliat, P. Coïsson, F. Civet, A. Du, A. Fournier, I. Fratter, N. Gillet, B. Hamilton, M. Hamoudi, G. Hulot, T. Jager, M. Korte, W. Kuang, X. Lalanne, B. Langlais, J.-M. Léger, V. Lesur, F. J. Lowes, S. Macmillan, M. Mandea, C. Manoj, S. Maus, N. Olsen, V. Petrov, V. Ridley, M. Rother, T. J. Sabaka, D. Saturnino, R. Schachtschneider, O. Sirol, A. Tangborn, A. Thomson, L. Tøffner-Clausen, P. Vigneron, I. Wardinski, and T. Zvereva. International Geomagnetic Reference Field: the 12th generation. *Earth, Planets and Space*, 67(1), May 2015.
- [34] J. Zhang, A. Lan, J. Yan, X. Deng, W. Wang, H. Li, L. Sun, Y. Nan, X. Song, and C. Wang. Development of the Chinese Dual Auroral Radar Network and Preliminary Results. *Space Weather*, 22(10):e2024SW004131, 2024. e2024SW004131 2024SW004131.